NANO LETTERS

pubs.acs.org/NanoLett Letter

A Power-Efficient Coplanar Waveguide Design for Enhanced Optical Readout in h-BN Quantum Sensors

Songtao Wu,[#] Biswajit Sahoo,[#] Naveed Hussain,[#] Alejandro Ruiz, Sumukh Vaidya, Saakshi Dikshit, Hayate Yamano, Katsunori Danno, Chen Ling, Shougo Higashi, Tongcang Li, and Debasish Banerjee*

Cite This: *Nano Lett.* 2025, 25, 11283−11290 Read Online

ACCESS | Metrics & More | Article Recommendations | Supporting Information

ABSTRACT: The past decade has witnessed a growing research interest in quantum sensing using spin-active boron vacancy (V_B^-) defects in hexagonal boron nitride (hBN). While hBN enables easy chip integration, current quantum sensing devices suffer from low optical readout and noisy signals due to inefficient waveguide designs that limit microwave absorption, resulting in reduced optically detected magnetic resonance (ODMR) contrast. This study advances hBN-integrated quantum sensors through three generations, culminating in a compact single-port coplanar waveguide (CPW). Unlike conventional two-port waveguides, our design allows on-chip optical and microwave excitation, ensuring improved impedance stability and high radio frequency (RF) magnetic field concentration without altering spin properties. As a result, we achieve a high ODMR contrast of ∼28% at low microwave power (MW) of 400 mW. This miniaturized sensor enhances efficiency three times, reduces the use of RF power to five times, and supports robust performance at lower MW power, making it ideal for scalable quantum sensing applications such as magnetic field detection.

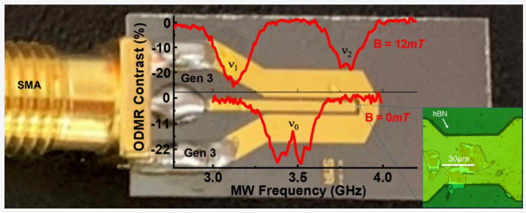

KEYWORDS: *hBN, spin defect, quantum sensor, coplanar waveguide, optically detected magnetic resonance*

Solid-state spin active defects such as nitrogen-vacancy (NV^-) centers in diamond,[1,2] carbon (V_c), and silicon (V_{Si}) defects in silicon carbide (SiC),[3−5] and more recently, negatively charged boron vacancy (V_B^-) defects in hexagonal boron nitride (hBN)[6−8] are critical for the development of quantum sensing. Unlike diamond and SiC, which are three-dimensional (3D) bulk materials, hBN is a two-dimensional (2D) van der Waals (*vdW*) layered material that enables easy exfoliation and hosts V_B^- spin defects, operating at room temperature. Well-established techniques like ion implantation,[9,10] electron irradiation,[11] and femtosecond laser writing[12] can be employed to create an ensemble of V_B^- defects at a controlled depth from the surface.[13] Furthermore, V_B^- defects are temperature-resilient (up to 600 °C)[14] and can be characterized using concurrent laser and microwave (MW) fields, aided by embedded fiber optics and waveguides. The response can be read optically at room temperature by optically detected magnetic resonance (ODMR),[6,15] eliminating the need for a complex setup.

The V_B^- spin defects in hBN have demonstrated significant potential for localized sensing of electrical, magnetic, and thermal fluxes within solid-state materials, emphasizing its potential for transformative device applications.[16] Experimental validation through confocal and wide-field optical microscopy platforms confirms hBN as a promising material for quantum technologies such as quantum sensing.[15,17−22] Specifically, hBN-based quantum sensors offer excellent integration with optoelectronics, photonics, and CMOS architectures due to their flexibility, enabling accelerated scalability compared to their rigid counterparts and allowing precise control of their response through physical stimuli such as temperature, pressure, and strain.[18]

The performance of a quantum sensor harnessing optically active spin defects is typically assessed using ODMR, which depends on the efficient detection of subtle changes in the photoluminescence (PL) signal as a function of the driving MW frequency. On resonance, MW can drive electron state transitions, which can lead to a change in the PL signal, showing up as a contrast when comparing cases with and without MW driving. Most ODMR demonstrations use conventional cavity resonators[23] and two-port (through-line) coplanar waveguides,[6,16,24] which rely on MW transmission and exhibit significantly reduced sensitivity to small frequency changes due to limited MW absorption. Furthermore, the inherent low brightness of V_B^- defects in hBN[16,21] complicates detection, requiring high laser fluence. This leads to reduced resolution, increased noise, heat buildup, and potential sample damage. Thus, a novel waveguide design is highly desired to address these issues.

Received: April 23, 2025
Revised: June 10, 2025
Accepted: July 3, 2025
Published: July 9, 2025

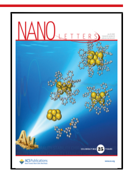

https://doi.org/10.1021/acs.nanolett.5c02316
Nano Lett. 2025, 25, 11283−11290

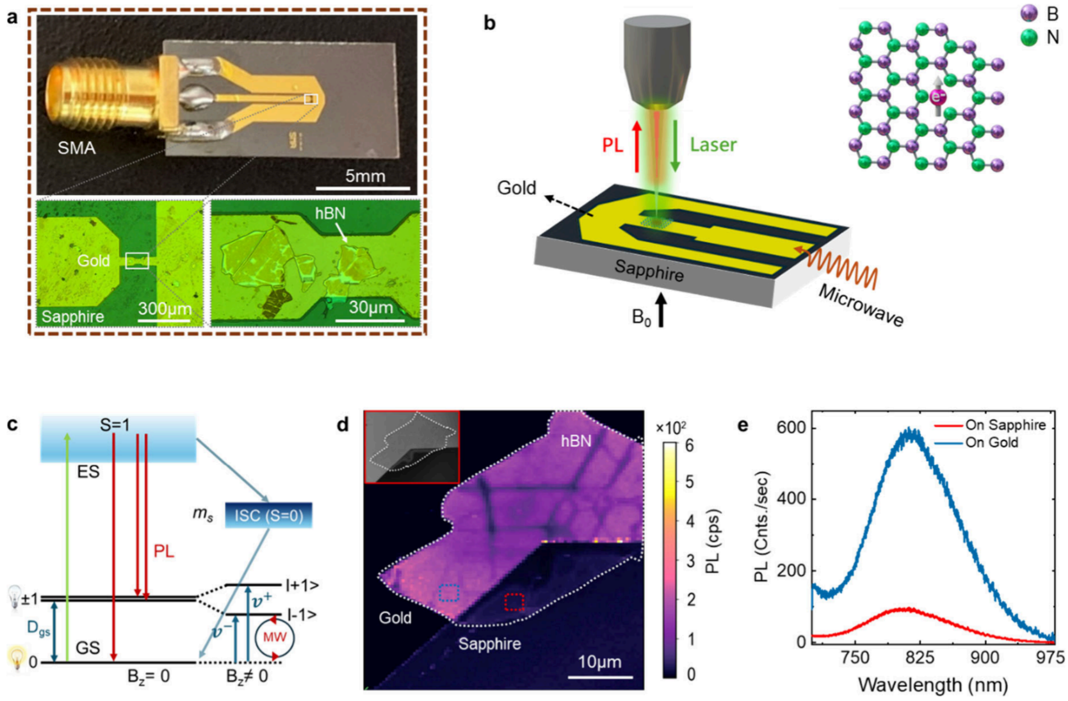

Figure 1. (a) The Gen 3 waveguide device with the zoomed-in figures showing the transferred hBN flakes on the constricted region. (b) Illustration of the experimental setup for PL and ODMR measurements. (c) The energy level diagram of a V_B^- defect and the optical pumping cycle between the ground state (GS), the excited state (ES), and the intersystem crossing state (ISC). (d) The confocal PL imaging of V_B^- implanted hBN flake showing plasmonic enhancement from the hBN lying on top of the gold waveguide, compared to the one resting over sapphire substrate. (e) The PL spectra V_B^- ensemble in hBN lying on gold (blue) and sapphire (red). The regions are highlighted by the corresponding blue and red dotted rectangles in (d).

In this work, we attempt to solve these challenges by adopting a modified waveguide design for efficient quantum sensing. A single-port waveguide design relies on MW reflection and offers the detection of subtle variations in resonance behavior as a result of efficient MW absorption and superior magnetic field sensitivity. We design and fabricate a shorted, constricted single-port coplanar waveguide (CPW), which enables seamless integration of hBN with combined optical and MW excitation. Multiphysics simulations carried out using COMSOL confirm better impedance stability and a high radio frequency (RF) magnetic field concentration of single-port CPW, twice as strong as conventional through-line CPWs (Gen 1: Transmission waveguide (TW)), enabling better signal-to-noise ratio (SNR) at lower MW power. We then fabricated devices based on substrate optimization, adopting a single-port CPW design on Si/SiO_2 (Gen 2) and sapphire (Gen 3) substrates to experimentally validate the design performance. We demonstrate a systematic improvement in the optical readout from Gens 1−3, where our Gen 3 device achieves an ODMR contrast of ∼28%, enabling energy efficiency and preservation of peak width resolution. Furthermore, we show a substantial ∼3-fold enhancement in the photoluminescence (PL) of V_B^- defects in the Gen 3 device by optimizing the surface characteristics of the sensor, resulting in improved DC magnetic field sensitivity (η_{DC}) of the Gen 3 device. We further investigate the intrinsic spin properties of the V_B^- ensemble coupled with Gen 3 device by measuring the spin−lattice relaxation time (T_1) and spin coherence time (T_2). These findings highlight the potential for practical, energy-efficient, robust, and compact quantum sensing devices.

Figure 1a shows the Gen 3 quantum sensing device, connected to a standard coaxial RF (SMA) connector and integrated with hBN. The creation of a spin-active ensemble of the V_B^- defects in mechanically exfoliated hBN flakes on a Si/SiO_2 substrate was performed by helium ion (He^+) irradiation. The irradiated flakes were then deterministically transferred to the restricted region of the prefabricated CPW structures (the magnified optical images) by the polymer-based dry transfer method. The schematic in Figure 1b shows the V_B^- defects associated with the optical excitation and readout processes. We excite the V_B^- defects using a 532 nm laser and collect the emitted photons. Akin to the NV^- center in diamond, the V_B^- center is a spin-1 ($S = 1$) system with triplet ground and excited states (see details in the Supporting Information). Figure 1c illustrates a simplified energy level diagram for the V_B^- center. The ground-state Hamiltonian of the V_B^- center in an external magnetic field B_z can be expressed as[25]

$$H = D_{gs}\left(\mathbf{S}_z^2 - \frac{S(S+1)}{3}\right) + E_{gs}(\mathbf{S}_x^2 - \mathbf{S}_y^2) + \gamma_e B_z \mathbf{S}_z \quad (1)$$

Here, $D_{gs} \approx 3.48$ GHz is the zero field-splitting parameter, $E_{gs} \approx 48\ MHz$ is the transverse ZFS parameter, and $\gamma_e \approx 28^{MHz}/_{mT}$ is the electron-spin gyromagnetic ratio. $\mathbf{S}$, $\mathbf{S}_x$, $\mathbf{S}_y$, and $\mathbf{S}_z$ denote the electron spin operators, and B_z is the out-of-plane component of the magnetic field. The application of microwaves allows the manipulation of the electron spin between the $m_s = 0$ and $m_s = \pm 1$ spin sublevels. Confocal PL imaging of an hBN flake overlapping a gold waveguide and sapphire revealed a strong plasmonic coupling between the V_B^- ensemble and the underlying gold, resulting in enhanced photoluminescence, eventually leading to better device performance (Figure 1d).[24] The PL spectra obtained from the V_B^- ensemble in hBN lying on the flat gold and sapphire are

https://doi.org/10.1021/acs.nanolett.5c02316
Nano Lett. 2025, 25, 11283−11290

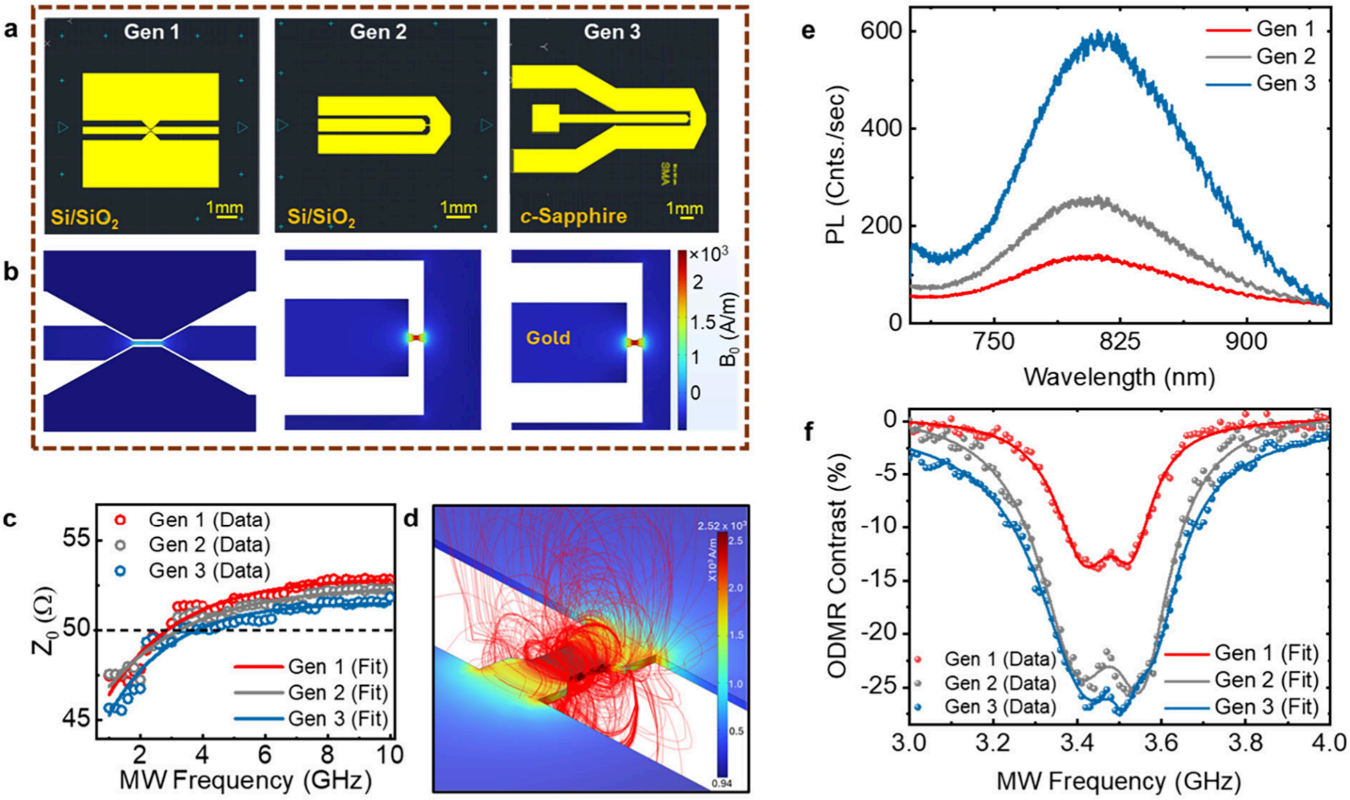

Figure 2. (a) The designs and (b) the finite element simulations of the Gen 1, 2, and 3 devices, respectively. The magnetic field intensity at the gold stripline of each of the devices has been presented. The field strength values for Gen 2 and 3 were close, approximately double that of Gen 1. The highest magnetic field values for Gen 1, 2, and 3 devices we obtained were 1037, 2390, and 2520 A/m, respectively, at a frequency of 3 GHz and an RF power of 1 W. (c) The impedance characteristics of CPWs as a function of MW frequency. The impedance is stable for Gen 2 and 3 over the working frequency range (2−4 GHz). (d) The field line distribution for the Gen 3 device. Most field lines are parallel to the hBN plane, even up to 30 μm. (e) The PL spectra of V_B^- defects, acquired from Gen 1, 2, and 3 at room temperature. (f) The ODMR contrasts of V_B^-ensemble for three Gen devices at an external magnetic field of 0 mT.

shown in Figure 1e. The two spectra were acquired from the regions of the hBN highlighted by the corresponding blue (hBN on the gold waveguide) and red (hBN on sapphire) dotted rectangles and show evidence of strong PL enhancement due to plasmonic coupling of the V_B^- defects with gold.

Figure 2 presents the designs and the corresponding COMSOL simulation results for three generations (Gen 1−3) of the physical quantum sensing devices fabricated on various substrates. Contrary to the typical two-port through-line waveguide design, adopted for the Gen 1 device, we opted for a shorter CPW design due to its inductive nature and minimal parasitic effects compared to through-line CPWs.[26] The inductive nature implies a much larger generation and storage of magnetic fields,[27,28] which is crucial for providing larger driving RF fields, enabling a better ODMR response. The constricted waveguide design, which imposes specific boundary conditions, leads to stronger field confinement. Unlike the case of through-line CPWs, the shorted CPW is designed with a self-impedance of 50 Ω, eliminating the need for an additional 50 Ω termination, allowing pathways for robust miniaturization. Additionally, the shorted CPW exhibits lower losses than the former, allowing for an energy-efficient device design.[29]

We simulated the RF characteristics; namely the impedance and the magnetic field intensity of through-line and shorted CPWs on Si/SiO_2, Si/SiO_2 and sapphire substrates. The computer-aided designs (CAD) of Gen 1, 2, and 3 devices have been presented in Figure 2a. Simulations were carried out in COMSOL Multiphysics in a frequency range of 1−10 GHz (Figure 2b). The Gen 1, 2, and 3 devices were fabricated on Si/SiO_2, Si/SiO_2 and *c*-sapphire substrates, respectively, where a Gen 3 device is shown alongside a one-cent coin for scale in Figure S1, Supporting Information. Notably, the device parameters can be adjusted to achieve a desired characteristic impedance, such as the 50 Ohms used in this study. The signal line width has been kept constant at 200 μm, whereas the slot width (i.e., the distance between signal and ground lines) has been adjusted to have close to 50 Ω impedance at 3 GHz with values of 140, 145, and 155 μm for Gen 1, 2, and 3 respectively.

The simulations were carried out within the same volume of 2500 × 1500 × 1000 μm^3 with a fixed substrate thickness of 500 μm. All three devices exhibited robust impedance stability throughout the entire frequency range, with a standard deviation of 10% from the targeted 50 Ω, with the Gen 3 device showing the closest match in the preferred MW frequency range of 2−6 GHz for the ODMR measurement (Figure 2c). The deviations at lower frequencies are generally associated with larger losses in these CPWs. More importantly, Gen 2 and 3 devices show a 2-fold increase in the magnetic field concentration for the same dimensions of the active region as opposed to Gen 1. The optimal accumulation of the RF magnetic field around the shorted antenna, at varying MW powers, has been simulated and presented as Figure S2,

https://doi.org/10.1021/acs.nanolett.5c02316
Nano Lett. 2025, 25, 11283−11290

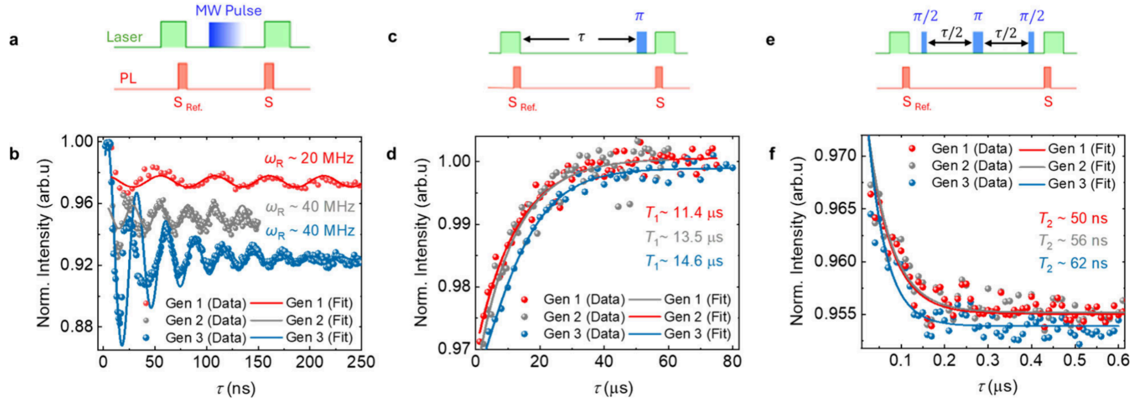

Figure 3. (a) Schematic of the Rabi oscillation measurement protocol. The duration of the blue MW pulse is modulated, and the PL is collected as shown in the diagram. (b) Collected Rabi oscillation data for devices Gen 1, Gen 2, and Gen 3 devices. (c) Schematic of the T_1 measurements performed. The state is initialized to the state $m_s = 0$, and its decay is monitored as a function of time. (d) Collected T_1 data of Gen 1, Gen 2, and Gen 3 devices. (e) Hahn Echo pulse sequence for measuring the T_2 of the qubits. After initialization into $m_s = 0$, the state is put into superposition with a $\frac{\pi}{2} - \pi - \frac{\pi}{2}$ sequence with increasing duration between pulses. (f) Measured T_2 data for Gen 1, Gen 2, and Gen 3 devices.

Supporting Information. This improved performance can be attributed to the inductive nature of shorted CPWs compared to the capacitive nature of through-line CPWs,[26] which can store and generate larger magnetic fields. This enhanced magnetic field strength is crucial for achieving proper alignment of the external driving field, a critical factor for generating strong readout signals from the V_B^- defects. Notably, the simulations also reveal that the magnetic field lines in Gen 2 and 3 remain parallel to the waveguide surface even up to 30 μm (Figure 2d). This parallel alignment further ensures an optimal interaction between the MW magnetic field and the V_B^- spins, resulting in better contrast in the readout of the spin state.

Upon excitation, the V_B^- center can decay via two pathways: a radiative transition resulting in PL emission in the range of 800−850 nm, or a nonradiative intersystem crossing (ISC). The PL spectra obtained from devices Gen 1, 2, and 3 have been presented in Figure 2e. The Gen 1 device displayed a weak PL signal, while the Gen 2 device (with CPW design) exhibited a relatively enhanced PL signal. This could be attributed to the lower effective dielectric constant (ε_{eff}), which reduces energy loss and substrate heating by electromagnetic field confinement, effectively suppressing nonradiative recombination and thermal quenching. However, the PL counts for the Gen 3 device further increased ∼3-fold compared to Gen 2, which we speculate to be associated with a higher surface roughness of the sapphire substrate (6−8 Å)[30] (enabling more contact with gold surface for plasmonic enhancement) compared to the Si/SiO_2 substrate (1 Å),[31] and its better heat buildup management,[32] as the PL responses are strongly coupled with the thermophysical properties of the underlying substrate.[33] Continuous wave (*cw*) ODMR measurements have been performed to acquire the basic spin characteristics of the V_B^- defects ensemble. The defects are excited by a 532 nm laser with an objective lens of NA = 0.9, which also collects the PL associated with V_B^- defects. We recorded the integrated photon counts as a function of the applied MW and quantified the differential response of the V_B^- defects by analyzing the difference in photon count rates between the microwave off (I_{off}) and microwave on (I_{on}) states. The ODMR contrast (C) is then determined by normalizing the PL difference with the PL intensity when the MW is off: $C = (I_{\text{on}} - I_{off})/I_{off}$. A negative contrast C of the *ODMR* means that the MW driving decreases the PL intensity.

Figure 2f shows the ODMR contrast obtained from Gen 1−3 devices without an external magnetic field. The ODMR of Gen 1 and Gen 2 devices was performed at a MW power of 2W, while that of Gen 3 was performed at a much lower power of 400 mW due to signal saturation at higher power. The measured ODMR spectrum for the Gen 1 device revealed two distinct resonances, ν_1, and ν_2, bracketing a central frequency, ν_0. This central frequency, ν_0, aligns closely with the zero-field splitting (ZFS) value of approximately 3.48 GHz. The splitting between ν_1 and ν_2 is due to the nonzero off-axial ZFS parameter E_{gs}/h = 50 MHz (h being the Planck constant). The ODMR contrast achieved in Gen 1 device was approximately 12%. However, transitioning to a single-port design in the Gen 2 device significantly improved the contrast of ODMR to around 26%. This enhancement is attributed to the optimized design, which allows for a more efficient coupling of microwave radiation to the spin defects and agrees with our simulation results. However, the resolution is compromised because the line width power broadening at high driving fields. This is evidenced by the softening of the two distinct peaks. For the Gen 3 device, we observed the highest ODMR contrast of 28%, along with well-defined off-axial ZFS peaks at a low MW power of 400 mW, which is just 20% of the maximum power capacity. The ODMR contrast obtained at different microwave powers for the three generations of devices is presented in Figure S3, Supporting Information. The retention of such high ODMR contrast of Gen 3 compared to Gen 2, particularly at lower MW power, can be attributed to the significantly lower loss tangent of sapphire (0.00002) compared to silicon (0.004).[34,35] The low-loss tangent of sapphire minimizes radiative losses and ensures efficient delivery of MW power directly to the defects, while simultaneously reducing the thermal deterioration of the obtained signal. The overall results demonstrate that the successful preservation of sensitivity alongside exceptionally high ODMR contrast can be associated with the optimal alignment of the RF magnetic field perpendicular to the quantization axis (*c*-axis). Miniaturization with this design is achievable, as demonstrated in our Gen 2 sensing device (Figure S4(a, b), Supporting Information), where over 200 coplanar waveguides (CPWs) fit within a 1 cm × 1 cm area. In Gen 3, we intentionally extended the

https://doi.org/10.1021/acs.nanolett.5c02316
Nano Lett. 2025, 25, 11283−11290

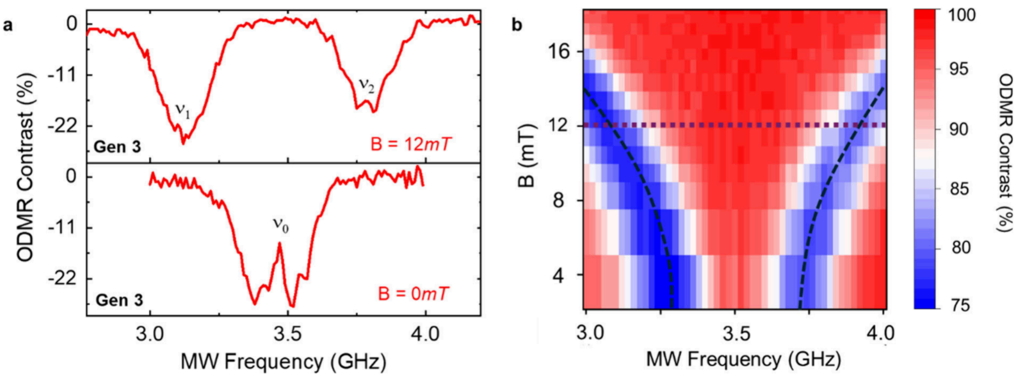

Figure 4. (a) ODMR spectra measured at zero magnetic field (bottom) and magnetic field B = 12 mT (top) with the corresponding ODMR frequencies, ν_0, ν_1, and, ν_2, respectively. (b) ODMR frequencies as a function of the magnetic field (B | | c). The experimental data (blue) and the fit (dotted black line) have been obtained using eq 2 with parameters D/h = 3.48 GHz, E/h = 50 MHz, and g = 2.000. The purple dashed line represents the position of the left ODMR spectrum at B = 12 mT.

dimensions of G, D, and S to facilitate a standard SMA connector for convenient lab handling. An argument can be made that the significantly greater length of the shorted antenna in Gen 1, compared to Gen 2 and Gen 3, could potentially contribute to the observed reduction in MW radiation density. To address this, we conducted COMSOL Multiphysics simulations in which we intentionally maintained a constant antenna footprint of 100 × 50 μm for both the open (Gen 1) and shorted (Gen 2 and Gen 3) antenna designs, using identical signal and ground line thicknesses. The simulations reveal that the shorted antenna design produces a 2-fold increase in the peak magnetic field (1640 A/m) compared to 837 A/m for the open antenna under the identical simulation area, antenna volume and input RF power conditions (see Figure S5 (a, b), Supporting Information). Furthermore, introducing a 30 × 30 μm constriction reduces the overall volume of the antenna and leads to a further enhancement in the magnetic field strength, reaching 2520 A/m, as expected (Figure S5 (c)). These results highlight the role of inductive effects in short waveguides for enhancing magnetic field strength,[28] reinforcing their suitability for robust quantum sensor design, as also demonstrated in hybrid quantum systems.[27]

To understand the impact of the CPW device on the spin properties of V_B^-spin defect, we performed pulsed ODMR measurement protocol to determine the spin−lattice relaxation time T_1 and the spin coherence time T_2 for all three devices. Response of the device to pulsed ODMR experiments will act as a precursor to more complex sensing protocols.[36,37] The ground state is optically initialized with a laser pulse, which is then subsequently manipulated coherently with MW pulses. Then a second laser pulse is employed to optically read the final spin state. Here we added an external magnetic field of 12 mT to split two branches of the V_B^- spin sublevels. The m_s = 1, 0 states are used as the two-level spin system to perform the spin-coherent control. Figure 3a and b respectively show the pulse schematic and contrast for Rabi oscillations for the three devices. The data is fit to the function $A \sin(\omega t + \phi) \exp(-t/\tau) + c$ to extract the Rabi oscillation frequency and the Rabi coherence time. The ω_R for Gen 2 and 3 devices is double that of Gen 1 indicating a roughly 2-fold increase in the incident MW amplitude on the samples. Furthermore, the Gen 2 and 3 devices show a similar ω_R, indicating aindicating similar MW power impinging on the V_B^-defects, corroborating the results observed in the simulations (Figure 3b). Despite the fact that the RF power applied to Gen 3 is ∼80% (or 7 dB) less than that of Gen 2, we can see a drastic improvement in signal quality for the Gen 3 device. These results indicate efficient MW power delivery to the V_B^-defects in the Gen 3 device at very low input MW power. Figures 3c and 3e show the pulse sequences used to measure the T_1 and T_2 times, respectively. From the fittings $A\exp\left(-\frac{t}{T_1}\right) + B$ and $A\exp\left(-\frac{t}{T_2}\right) + B$ in Figure 3 d and f, T_1 and T_2 show similar values for the three devices, with Gen 3 having slightly higher values (14.6 μs and 62 ns, respectively). This implies that our CPW design does not influence the intrinsic spin characteristics of V_B^-defects.

Figure 4a demonstrates the sensing of the external magnetic field using the Gen 3 device following the electron spin resonance (ESR) measurement. The evolution of the ODMR spectrum for hBN when an external magnetic field is applied parallel to its hexagonal *c*-axis has been presented. To mitigate heat build-up that could influence the accuracy of the measurements, we intentionally kept reduced laser (400 μW) and microwave power (200 mW) during the ESR measurements, resulting in a lower ODMR contrast. The observed transitions and their field-dependent behavior can be explained using the standard spin Hamiltonian (eq 1), where the *z*-axis aligns with the *c*-axis of the hBN crystal. Based on eq 1, with B applied parallel to the *c*-axis, the resonant MW frequencies for transitions vary as

$$\nu_{1,2} = \nu_0 \pm \frac{1}{h}\sqrt{E^2 + (g\mu_B B)^2} \tag{2}$$

Here, $\nu_0 = D/h$. The ESR map, which presents the frequency splitting between $\boldsymbol{\upsilon}_1$ and $\boldsymbol{\upsilon}_2$ as a function of MW frequency at varying external magnetic field applied along the long axis of the crystal, has been shown in Figure 4b. This splitting can be precisely modeled using eq 2, which indicates a highly symmetrical, nearly uniaxial defect structure.

ODMR spectroscopy is a primary technique for estimating the η_{DC} of V_B^- spin defects in hBN. Despite technical noise and measurement uncertainties, the η_{DC} can be characterized by its shot-noise-limited sensitivity[38]

$$\eta_{DC} = \frac{4}{3\sqrt{3}}\frac{h}{g\mu_B}\frac{\Delta\nu}{C\sqrt{I}} \tag{3}$$

https://doi.org/10.1021/acs.nanolett.5c02316
Nano Lett. 2025, 25, 11283−11290

where $\Delta\nu$, C, and I represent the ODMR line width, ODMR contrast, and PL count rate, respectively. h is Planck's constant, $g \approx 2$ is the Landé g factor, and μ_B is the Bohr magneton.

Due to the relatively short coherence time of the V_B^- ensemble, leading to an indistinguishable ODMR spectral line shape,[39,40] individual resonance peaks must be resolved using the Lorentzian model (eq 4) to fit the ODMR spectrum and extract $\Delta\nu$:

$$I(\nu) = a + b \times \frac{\frac{\Delta\nu}{2}}{(\nu - \nu_0)^2 + \left(\frac{\Delta\nu}{2}\right)^2} \tag{4}$$

where a, b are fitting parameters, $\Delta\nu$ is the line width of the transition, and ν_0 is the center frequency of the transition. Based on eq 3, the η_{DC} for Gen 1, 2, and 3 devices was estimated to be 368, 117.7, and 72.7 $\mu T/\sqrt{Hz}$, respectively, under the same magnetic field (see Table 1, Supporting Information). This indicates that our Gen 3 devices exhibit >5-fold enhancement in η_{DC}, compared to Gen 1 device. This enhancement factor has been achieved by optimizing all variables, including the line width ($\Delta\nu$), contrast (C), and PL intensity (I).

In conclusion, we propose an efficient hBN-integrated quantum sensing device that exhibits excellent ODMR performance at low RF power of 400 mW, by adopting a single-port shorted coplanar waveguide (CPW) design, fabricated on a sapphire substrate. Superior MW coupling with V_B^- spin defects and low-loss tangent of sapphire substrate resulted in an optimal ODMR contrast of 28% and higher PL (cps) in our Gen 3 device, achieving a high η_{DC} of 72.7 $\mu T/\sqrt{Hz}$. This represents a 5-fold improvement over conventional two-port designs (Gen 1). The technology presented offers a compelling combination of compactness, simplicity of design, and energy efficiency. In particular, it also achieves a high signal-to-noise ratio (SNR), which is crucial for reliable operation in environments with significant background noise. These attributes, particularly the miniaturization, and high optical readout at low power consumption, render this technology a promising candidate for future integration into robust quantum sensing applications.

ASSOCIATED CONTENT

Supporting Information

The Supporting Information is available free of charge at https://pubs.acs.org/doi/10.1021/acs.nanolett.5c02316.

Methods, ion-implantation scheme, hBN transfer procedure, and additional details of the ODMR measurement scheme and the confocal microscopy, along with some additional results from COMSOL simulation and demonstration of scalability on a Si wafer (PDF)

AUTHOR INFORMATION

Corresponding Author

Debasish Banerjee − *Toyota Research Institute of North America, Ann Arbor, Michigan 48105, United States;* Email: Debasish.banerjee@toyota.com

Authors

Songtao Wu − *Toyota Research Institute of North America, Ann Arbor, Michigan 48105, United States*

Biswajit Sahoo − *Toyota Research Institute of North America, Ann Arbor, Michigan 48105, United States; Department of Physics, University of California, San Diego, California 92093, United States;* orcid.org/0000-0001-5126-1962

Naveed Hussain − *Toyota Research Institute of North America, Ann Arbor, Michigan 48105, United States;* orcid.org/0000-0003-2567-5066

Alejandro Ruiz − *Toyota Research Institute of North America, Ann Arbor, Michigan 48105, United States*

Sumukh Vaidya − *Department of Physics and Astronomy, Purdue University, Indiana 47907, United States;* orcid.org/0000-0002-9732-6829

Saakshi Dikshit − *Elmore Family School of Electrical and Computer Engineering, Purdue University, West Lafayette, Indiana 47907, United States*

Hayate Yamano − *Material Engineering Division, Toyota Motor Corporation, Aichi, Japan 471-8572*

Katsunori Danno − *Material Engineering Division, Toyota Motor Corporation, Aichi, Japan 471-8572*

Chen Ling − *Toyota Research Institute of North America, Ann Arbor, Michigan 48105, United States;* orcid.org/0000-0002-8667-9792

Shougo Higashi − *Toyota Research Institute of North America, Ann Arbor, Michigan 48105, United States; Material Engineering Division, Toyota Motor Corporation, Aichi, Japan 471-8572*

Tongcang Li − *Department of Physics and Astronomy, Purdue University, Indiana 47907, United States; Elmore Family School of Electrical and Computer Engineering, Purdue University, West Lafayette, Indiana 47907, United States;* orcid.org/0000-0003-3308-8718

Complete contact information is available at: https://pubs.acs.org/10.1021/acs.nanolett.5c02316

Author Contributions

#Songtao Wu, Biswajit Sahoo, and Naveed Hussain contributed equally to this work.

Notes

The authors declare no competing financial interest.

REFERENCES

(1) Doherty, M. W.; Manson, N. B.; Delaney, P.; Jelezko, F.; Wrachtrup, J.; Hollenberg, L. C. L. The Nitrogen-Vacancy Colour Centre in Diamond. *Phys. Rep.* **2013**, *528* (1), 1−45.

(2) Degen, C. L.; Reinhard, F.; Cappellaro, P. Quantum Sensing. *Rev. Mod. Phys.* **2017**, *89* (3), No. 035002.

(3) Csóré, A.; Son, N. T.; Gali, A. Towards Identification of Silicon Vacancy-Related Electron Paramagnetic Resonance Centers in 4H-SiC. *Phys. Rev. B* **2021**, *104* (3), No. 035207.

(4) Falk, A. L.; Buckley, B. B.; Calusine, G.; Koehl, W. F.; Dobrovitski, V. V.; Politi, A.; Zorman, C. A.; Feng, P. X.-L.; Awschalom, D. D. Polytype Control of Spin Qubits in Silicon Carbide. *Nat. Commun.* **2013**, *4* (1), 1819.

(5) Riedel, D.; Fuchs, F.; Kraus, H.; Väth, S.; Sperlich, A.; Dyakonov, V.; Soltamova, A. A.; Baranov, P. G.; Ilyin, V. A.; Astakhov, G. V. Resonant Addressing and Manipulation of Silicon Vacancy Qubits in Silicon Carbide. *Phys. Rev. Lett.* **2012**, *109* (22), No. 226402.

(6) Gottscholl, A.; Kianinia, M.; Soltamov, V.; Orlinskii, S.; Mamin, G.; Bradac, C.; Kasper, C.; Krambrock, K.; Sperlich, A.; Toth, M.; Aharonovich, I.; Dyakonov, V. Initialization and Read-out of Intrinsic Spin Defects in a van Der Waals Crystal at Room Temperature. *Nat. Mater.* **2020**, *19* (5), 540−545.

(7) Mendelson, N.; Chugh, D.; Reimers, J. R.; Cheng, T. S.; Gottscholl, A.; Long, H.; Mellor, C. J.; Zettl, A.; Dyakonov, V.; Beton,

P. H.; Novikov, S. V.; Jagadish, C.; Tan, H. H.; Ford, M. J.; Toth, M.; Bradac, C.; Aharonovich, I. Identifying Carbon as the Source of Visible Single-Photon Emission from Hexagonal Boron Nitride. *Nat. Mater.* **2021**, *20* (3), 321−328.

(8) Stern, H. L.; Gu, Q.; Jarman, J.; Eizagirre Barker, S.; Mendelson, N.; Chugh, D.; Schott, S.; Tan, H. H.; Sirringhaus, H.; Aharonovich, I.; Atatüre, M. Room-Temperature Optically Detected Magnetic Resonance of Single Defects in Hexagonal Boron Nitride. *Nat. Commun.* **2022**, *13* (1), 618.

(9) Kianinia, M.; White, S.; Fröch, J. E.; Bradac, C.; Aharonovich, I. Generation of Spin Defects in Hexagonal Boron Nitride. *ACS Photonics* **2020**, *7* (8), 2147−2152.

(10) Guo, N.-J.; Liu, W.; Li, Z.-P.; Yang, Y.-Z.; Yu, S.; Meng, Y.; Wang, Z.-A.; Zeng, X.-D.; Yan, F.-F.; Li, Q.; Wang, J.-F.; Xu, J.-S.; Wang, Y.-T.; Tang, J.-S.; Li, C.-F.; Guo, G.-C. Generation of Spin Defects by Ion Implantation in Hexagonal Boron Nitride. *ACS Omega* **2022**, *7* (2), 1733−1739.

(11) Murzakhanov, F. F.; Yavkin, B. V.; Mamin, G. V.; Orlinskii, S. B.; Mumdzhi, I. E.; Gracheva, I. N.; Gabbasov, B. F.; Smirnov, A. N.; Davydov, V. Y.; Soltamov, V. A. Creation of Negatively Charged Boron Vacancies in Hexagonal Boron Nitride Crystal by Electron Irradiation and Mechanism of Inhomogeneous Broadening of Boron Vacancy-Related Spin Resonance Lines. *Nanomaterials* **2021**, *11* (6), 1373.

(12) Gao, X.; Pandey, S.; Kianinia, M.; Ahn, J.; Ju, P.; Aharonovich, I.; Shivaram, N.; Li, T. Femtosecond Laser Writing of Spin Defects in Hexagonal Boron Nitride. *ACS Photonics* **2021**, *8* (4), 994−1000.

(13) Gao, X.; Vaidya, S.; Ju, P.; Dikshit, S.; Shen, K.; Chen, Y. P.; Li, T. Quantum Sensing of Paramagnetic Spins in Liquids with Spin Qubits in Hexagonal Boron Nitride. *arXiv Preprint*, arXiv:2303.02326, 2023. DOI: 10.48550/ARXIV.2303.02326.

(14) Suzuki, T.; Yamazaki, Y.; Taniguchi, T.; Watanabe, K.; Nishiya, Y.; Matsushita, Y.; Harii, K.; Masuyama, Y.; Hijikata, Y.; Ohshima, T. Spin Property Improvement of Boron Vacancy Defect in Hexagonal Boron Nitride by Thermal Treatment. *Appl. Phys. Express* **2023**, *16* (3), 032006.

(15) Vaidya, S.; Gao, X.; Dikshit, S.; Aharonovich, I.; Li, T. Quantum Sensing and Imaging with Spin Defects in Hexagonal Boron Nitride. *Adv. Phys. X* **2023**, *8* (1), 2206049.

(16) Gottscholl, A.; Diez, M.; Soltamov, V.; Kasper, C.; Krauße, D.; Sperlich, A.; Kianinia, M.; Bradac, C.; Aharonovich, I.; Dyakonov, V. Spin Defects in hBN as Promising Temperature, Pressure and Magnetic Field Quantum Sensors. *Nat. Commun.* **2021**, *12* (1), 4480.

(17) Huang, M.; Zhou, J.; Chen, D.; Lu, H.; McLaughlin, N. J.; Li, S.; Alghamdi, M.; Djugba, D.; Shi, J.; Wang, H.; Du, C. R. Wide Field Imaging of van Der Waals Ferromagnet Fe_3GeTe_2 by Spin Defects in Hexagonal Boron Nitride. *Nat. Commun.* **2022**, *13* (1), 5369.

(18) Lyu, X.; Tan, Q.; Wu, L.; Zhang, C.; Zhang, Z.; Mu, Z.; Zúñiga-Pérez, J.; Cai, H.; Gao, W. Strain Quantum Sensing with Spin Defects in Hexagonal Boron Nitride. *Nano Lett.* **2022**, *22* (16), 6553−6559.

(19) Kumar, P.; Fabre, F.; Durand, A.; Clua-Provost, T.; Li, J.; Edgar, J. H.; Rougemaille, N.; Coraux, J.; Marie, X.; Renucci, P.; Robert, C.; Robert-Philip, I.; Gil, B.; Cassabois, G.; Finco, A.; Jacques, V. Magnetic Imaging with Spin Defects in Hexagonal Boron Nitride. *Phys. Rev. Appl.* **2022**, *18* (6), L061002.

(20) Gao, X.; Vaidya, S.; Li, K.; Ju, P.; Jiang, B.; Xu, Z.; Allcca, A. E. L.; Shen, K.; Taniguchi, T.; Watanabe, K.; Bhave, S. A.; Chen, Y. P.; Ping, Y.; Li, T. Nuclear Spin Polarization and Control in Hexagonal Boron Nitride. *Nat. Mater.* **2022**, *21* (9), 1024−1028.

(21) Gong, R.; He, G.; Gao, X.; Ju, P.; Liu, Z.; Ye, B.; Henriksen, E. A.; Li, T.; Zu, C. Coherent Dynamics of Strongly Interacting Electronic Spin Defects in Hexagonal Boron Nitride. *Nat. Commun.* **2023**, *14* (1), 3299.

(22) Durand, A.; Clua-Provost, T.; Fabre, F.; Kumar, P.; Li, J.; Edgar, J. H.; Udvarhelyi, P.; Gali, A.; Marie, X.; Robert, C.; Gérard, J. M.; Gil, B.; Cassabois, G.; Jacques, V. Optically Active Spin Defects in Few-Layer Thick Hexagonal Boron Nitride. *Phys. Rev. Lett.* **2023**, *131* (11), No. 116902.

(23) Colton, J. S.; Wienkes, L. R. Resonant Microwave Cavity for 8.5−12 GHz Optically Detected Electron Spin Resonance with Simultaneous Nuclear Magnetic Resonance. *Rev. Sci. Instrum.* **2009**, *80* (3), 035106.

(24) Gao, X.; Jiang, B.; Llacsahuanga Allcca, A. E.; Shen, K.; Sadi, M. A.; Solanki, A. B.; Ju, P.; Xu, Z.; Upadhyaya, P.; Chen, Y. P.; Bhave, S. A.; Li, T. High-Contrast Plasmonic-Enhanced Shallow Spin Defects in Hexagonal Boron Nitride for Quantum Sensing. *Nano Lett.* **2021**, *21* (18), 7708−7714.

(25) Zhou, F.; Jiang, Z.; Liang, H.; Ru, S.; Bettiol, A. A.; Gao, W. DC Magnetic Field Sensitivity Optimization of Spin Defects in Hexagonal Boron Nitride. *Nano Lett.* **2023**, *23* (13), 6209−6215.

(26) Beilenhoff, K.; Klingbeil, H.; Heinrich, W.; Hartnagel, H. L. Open and Short Circuits in Coplanar MMIC's. *IEEE Trans. Microw. Theory Technol.* **1993**, *41* (9), 1534−1537.

(27) Satzinger, K. J.; Conner, C. R.; Bienfait, A.; Chang, H.-S.; Chou, M.-H.; Cleland, A. Y.; Dumur, É.; Grebel, J.; Peairs, G. A.; Povey, R. G.; Whiteley, S. J.; Zhong, Y. P.; Awschalom, D. D.; Schuster, D. I.; Cleland, A. N. Simple Non-Galvanic Flip-Chip Integration Method for Hybrid Quantum Systems. *Appl. Phys. Lett.* **2019**, *114* (17), 173501.

(28) Wei, J.; Wang, J.; Liu, Q.; Li, X.; Cao, D.; Sun, X. An Induction Method to Calculate the Complex Permeability of Soft Magnetic Films without a Reference Sample. *Rev. Sci. Instrum.* **2014**, *85* (5), 054705.

(29) Ponchak, G. E.; Katehi, L. P. B. Open- and Short-Circuit Terminated Series Stubs in Finite-Width Coplanar Waveguide on Silicon. *IEEE Trans. Microw. Theory Technol.* **1997**, *45* (6), 970−976.

(30) Dallaeva, D.; Ţălu, Ş.; Stach, S.; Škarvada, P.; Tománek, P.; Grmela, L. AFM Imaging and Fractal Analysis of Surface Roughness of AlN Epilayers on Sapphire Substrates. *Appl. Surf. Sci.* **2014**, *312*, 81−86.

(31) Jeong, J. H.; Bae, J. S.; Yi, S.-S.; Park, J.-C.; Kim, Y. S. Photoluminescence Characteristics of Li-Doped Y2O3:Eu3+ Thin-Film Phosphors on Sapphire Substrates. *J. Phys.: Condens. Matter* **2003**, *15* (3), 567.

(32) Yamashita, Y.; Honda, K.; Yagi, T.; Jia, J.; Taketoshi, N.; Shigesato, Y. Thermal Conductivity of Hetero-Epitaxial ZnO Thin Films on c- and r-Plane Sapphire Substrates: Thickness and Grain Size Effect. *J. Appl. Phys.* **2019**, *125* (3), 035101.

(33) Kurbanov, S. S.; Igamberdiev, K. T.; Kang, T. W. The UV-Laser Induced Heating Effect on Photoluminescence from ZnO Nanocrystals Deposited on Different Substrates. *J. Phys. Appl. Phys.* **2010**, *43* (11), No. 115401.

(34) Li, D.; Gao, J.; Austermann, J. E.; Beall, J. A.; Becker, D.; Cho, H.-M.; Fox, A. E.; Halverson, N.; Henning, J.; Hilton, G. C.; Hubmayr, J.; Irwin, K. D.; Van Lanen, J.; Nibarger, J.; Niemack, M. Improvements in Silicon Oxide Dielectric Loss for Superconducting Microwave Detector Circuits. *IEEE Trans. Appl. Supercond.* **2013**, *23* (3), 1501204−1501204.

(35) Hartnett, J. G.; Tobar, M. E.; Ivanov, E. N.; Krupka, J. Room Temperature Measurement of the Anisotropic Loss Tangent of Sapphire Using the Whispering Gallery Mode Technique. *IEEE Trans. Ultrason. Ferroelectr. Freq. Control* **2006**, *53* (1), 34−38.

(36) Taylor, J. M.; Cappellaro, P.; Childress, L.; Jiang, L.; Budker, D.; Hemmer, P. R.; Yacoby, A.; Walsworth, R.; Lukin, M. D. High-Sensitivity Diamond Magnetometer with Nanoscale Resolution. *Nat. Phys.* **2008**, *4* (10), 810−816.

(37) Barry, J. F.; Schloss, J. M.; Bauch, E.; Turner, M. J.; Hart, C. A.; Pham, L. M.; Walsworth, R. L. Sensitivity Optimization for NV-Diamond Magnetometry. *Rev. Mod. Phys.* **2020**, *92* (1), No. 015004.

(38) Gao, X.; Vaidya, S.; Dikshit, S.; Ju, P.; Shen, K.; Jin, Y.; Zhang, S.; Li, T. Nanotube Spin Defects for Omnidirectional Magnetic Field Sensing. *Nat. Commun.* **2024**, *15* (1), 7697.

(39) Gottscholl, A.; Diez, M.; Soltamov, V.; Kasper, C.; Sperlich, A.; Kianinia, M.; Bradac, C.; Aharonovich, I.; Dyakonov, V. Room Temperature Coherent Control of Spin Defects in Hexagonal Boron Nitride. *Sci. Adv.* **2021**, *7* (14), No. eabf3630.

https://doi.org/10.1021/acs.nanolett.5c02316
Nano Lett. 2025, 25, 11283−11290

(40) Ramsay, A. J.; Hekmati, R.; Patrickson, C. J.; Baber, S.; Arvidsson-Shukur, D. R. M.; Bennett, A. J.; Luxmoore, I. J. Coherence Protection of Spin Qubits in Hexagonal Boron Nitride. *Nat. Commun.* **2023**, *14* (1), 461.

https://doi.org/10.1021/acs.nanolett.5c02316
Nano Lett. 2025, 25, 11283−11290